Applied Surface Science 716 (2026) 164667

Contents lists available at ScienceDirect

Applied Surface Science

journal homepage: www.elsevier.com/locate/apsusc

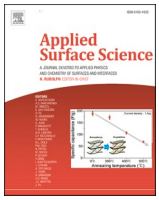

Full Length Article

Atomic layer deposition of alumina and zinc oxide nanofilms on ceria nanoparticles using a custom fluidized bed reactor for tunable ultraviolet blocking property

Guanghui Yan [a,*], Heng Yu [b], Lu Jin [a], Yi Ouyang [a], Guoxiang Chen [a], Gaoshan Huang [a,b], Xiangzhong Chen [a,b,c], Jizhai Cui [b], Xueqin Zuo [a,b], Zhihao Bao [a], Yongfeng Mei [a,b,c], Jianjun Shi [a,b,**]

[a] Zhejiang Key Laboratory of Extreme Environment Functional Materials, Yiwu Research Institute of Fudan University, Yiwu 322000, Zhejiang, PR China
[b] International Institute of Intelligent Nanorobots and Nanosystems & State Key Laboratory of Surface Physics, College of Intelligent Robotics and Advanced Manufacturing, Fudan University, Shanghai 200438, PR China
[c] Shanghai Frontiers Science Research Base of Intelligent Optoelectronics and Perception, Institute of Optoelectronics, Fudan University, Shanghai 200438, PR China

ARTICLE INFO

Keywords:
Ceria nanoparticle
Surface modification
Atomic layer deposition
Nanofilm
Fluidized bed reactor
UV blocking

ABSTRACT

Ceria (CeO_2) nanoparticles are considered potential ultraviolet (UV) absorbers for practical applications owing to their high absorption capability and long-term stability. However, there remain challenges in modulating their UV-blocking properties. Herein, we tailored the UV-blocking properties of CeO_2 nanoparticles through surface modification by depositing Al_2O_3 and ZnO nanofilms via atomic layer deposition (ALD) in a custom fluidized bed reactor. The absorption band blue-shifted from 3.34 eV (pristine) to 3.39 eV after 10 Al_2O_3 ALD cycles, whereas it red-shifted to 3.21 eV after 30 ZnO ALD cycles. The colors of ALD-modified nanoparticles changed from light yellow to light gray as the number of ALD cycles increased. XRD, HRTEM, element mapping, and XPS analysis were conducted and demonstrated that a uniform amorphous Al_2O_3 nanofilm with abundant oxygen vacancies coated the CeO_2 nanoparticle as a shell, forming a CeO_2@Al_2O_3 core@shell structure, whereas ALD-deposited ZnO nanofilms with high lattice oxygen content were crystalline and formed CeO_2/ZnO heterostructures at the interfaces. Based on valence band (VB) XPS, we proposed a band structure model to analyze the origin of the band shifts. This study demonstrates that ALD can effectively modulate the UV-absorption properties of CeO_2 nanoparticles, thereby enabling value-added utilization of high-abundance rare earth resources.

1. Introduction

Ultraviolet (UV) rays in sunlight, which can be divided into three parts, namely UVA (320–400 nm), UVB (280–320 nm), and UVC (200–280 nm) [1,2], are seem as very important factors which could produce skin cancer, accelerate skin aging, and induce other deleterious effects of human skin [3,4]. Because of the high photon energy, UV rays could cause sunburn and suntanning [3]. It is well known that sunburn is mainly caused by UVB rays, whereas suntanning is mainly caused by UVA rays [5]. Due to the protect of the atmosphere of Earth, most of UVC rays are impeded before they get to the surface of Earth [2]. To shield the UV rays, many organic UV absorbers and inorganic blocking materials are usually used in practical cosmetics [6–8]. Organic UV absorbers may degrade under long-term UV irradiation, cause safety problems such as skin allergies and dermatitis, and induce environment concerns [8,9]. Compared to organic absorbers, inorganic blocking materials such as rutile titanium dioxide (TiO_2), zinc oxide (ZnO), and ceria (CeO_2), show mild to skin, friendly to environment, and long-term stability [8].

As one of the high-abundance rare earth materials, CeO_2 has been widely investigated in the fields of antibacterial materials [10–12], chemical mechanical abrasives [13,14], and photo-catalysis [15,16]. Besides that, CeO_2 nanoparticles have attracted much attention for the applications in UV-blocking materials due to their large UV-absorption

* Corresponding author.
** Corresponding author at Zhejiang Key Laboratory of Extreme Environment Functional Materials, Yiwu Research Institute of Fudan University, Yiwu 322000, Zhejiang, PR China.
E-mail addresses: yangh@ywfudan.cn (G. Yan), Shijianjun@ywfudan.cn (J. Shi).

https://doi.org/10.1016/j.apsusc.2025.164667
Received 25 June 2025; Received in revised form 27 August 2025; Accepted 17 September 2025
Available online 20 September 2025

capability and long-term stability under UV irradiation [17]. The cubic CeO_2 has a theoretical band gap of ca. 3.1 eV [18,19]. According to the Planck-Einstein equation ($E = h\upsilon = hc/\lambda$), the relation between optical band gap (E_g) and absorption edge (λ) can be expressed as $E_g(eV) = \frac{hc}{e\lambda} \approx 1240/\lambda$, where the unit of λ is nm. Therefore, the cubic CeO_2 has an absorption band at about 400 nm, meaning that almost all UV light can be filtered by cubic phase CeO_2 nanoparticles. However, CeO_2-related materials still face the challenge in adjusting their UV-absorption capability for various UV-shielding requirements. Tuning of energy band gap is deemed as an effective way to adjust the UV-absorption property of CeO_2 nanoparticles. To tune the band-gap energies, doping of ions into CeO_2 via solution chemical routes is usually used. Using soft solution chemical routes, Yabe and Sato have doped serial M^+ ions into CeO_2 nanoparticles and found that Ca^{2+}- and Zn^{2+}-doped CeO_2 show high UV-absorption capability and high transparency in the visible spectrum [20]. Similarly, doping of transition metal ions (Co^{3+}, Zr^{4+}, and Cu^{2+}) by solution chemical method has been verified to adjust the energy band gap of CeO_2 [21]. Bao and co-worker have applied a modified sol–gel method to dope F^- and achieved F ion-doped CeO_2 nanoparticles with a blue shift of absorption band [22]. To extend the UV-shielding property, Li *et al.* have used solution chemical method to co-dope Sm and S and achieved CeO_2-based nanoparticles with absorption band in the blue light region (400–450 nm) [23]. Coating films on CeO_2 could also tune the UV-absorption property. Masui *et al.* have employed solution chemical method to coat turbostratic boron nitride (t-BN) on CeO_2 [5]. Additionally, size control is deemed as an effective way to adjust the band gap of CeO_2 nanoparticles [24]. The above-mentioned ways to adjust the band gap of CeO_2-related materials are commonly fabricated in the environment of aqueous solutions. Under this circumstance, the prepared CeO_2-based materials usually need to be washed and dried before using, which is deemed as a time-consuming process. Therefore, it is superior to the traditional solution chemical methods that tuning the absorption property of CeO_2 nanoparticles without solutions.

As a gaseous chemical reaction, atomic layer deposition (ALD) can deposit conformal, uniform, and atomic-level films on the substrates including particles due to the characteristic of self-limiting and self-saturated surface chemical reaction [25,26]. This characteristic results from the unique dosing manner in which gaseous reactants are sequentially pulsed into the reaction chamber and intermitted by a purging step of an inert gas [25]. Therefore, ALD is emerging as a promising technique for surface modifications of functional nanoparticles [27–29]. However, particles, especially nanoparticles, tend to attract each other and form agglomeration due to the strong attractive forces between them [30], which may reduce the interactions between gaseous reactants and surfaces of nanoparticles, thereby leaving the nanoparticles uncoated [31]. To separate nanoparticles effectively, many techniques such as rotation, vibration, and fluidization, have been used in particle ALD systems [31–35]. Among them, fluidization is considered a useful way to separate particles and has the ability in scale-up solutions [28,35]. Therefore, to tune the absorption property of CeO_2 nanoparticles, we utilize particle ALD technique to deposit Al_2O_3 and ZnO nanofilms on the nanoparticles in a gaseous process. The selection of Al_2O_3 and ZnO is based on: (1) the availability of ALD precursors and (2) their complementary properties (insulating vs. semiconducting). It is also worth noting that ZnO possesses diverse chemical optical, electronic, and magnetic properties, which is considered a promising material for user-friendly multifunctional devices [36–41].

In this study, a custom fluidized bed reactor (FBR) that is fully enclosed into a resistance wire furnace has been fabricated and assembled into a control cabinet to form a FBR-ALD system. CeO_2 nanoparticles with the diameter in the range of 20–50 nm are used as particle substrates in our study. With the set-up FBR-ALD, nanoscale Al_2O_3 and ZnO films are successfully deposited on CeO_2 nanoparticles. The phase structures, morphology, and chemical states of the deposited nanofilms are carefully observed via X-ray diffraction (XRD), high-resolution transmission electron microscopy (HRTEM), and X-ray photoelectron spectroscopy (XPS). The UV-absorption properties of the ALD-coated CeO_2 nanoparticles were conducted on a UV–vis–NIR spectrometer. The UV-absorption properties caused by different coatings are compared and discussed. This paper provides a gaseous method to modulate the UV-absorption properties of CeO_2 nanoparticles and could benefit the value-added utilization of the high-abundance cerium element.

2. Experimental details

2.1. Set-up of FBR-ALD

The particle ALD system used in this work was based on a homemade fluidized bed reactor, while the control cabinet was provided by Jiangsu MNT Micro and Nanotech Co. Ltd. The schematic diagram of FBR-ALD system is shown in Fig. 1. The reaction vessel that was used to functionalize the CeO_2 nanoparticles was made from 316L stainless steel with the inner diameter of 22 mm. The vessel was equipped with a removable 10–20 μm porous steel distributor plate at the inlet to support the particles and cylindrical filters at the outlet to prevent the particles from being extracted from the vessel. Pirani manometers (P_1 and P_2) were used to monitor the pressure state of the particle bed in the vessel while the Pirani manometer P_3 was used for monitoring the pressure of outlet. The inlet and outlet of the vessel were connected by Conflat (CF) flanges and sealed using copper gaskets. The whole vessel was placed inside a resistance furnace with a thermal couple (T) to monitor the reactor temperature. The left part in Fig. 1 represents dosing zones, consisting of main N_2 inlet line which can be regulated by a rotameter and two precursor lines which can be regulated by mass flow controller (MFC) using N_2 as the carrier gas. The precursor doses were controlled by high speed ALD valves (Swagelok company). PLC software was used to control precursor dosing by pneumatic valves. The whole photograph of set-up ALD system which consists of control cabinet, reactor, and furnace is displayed in Fig. S1 (Supporting Information).

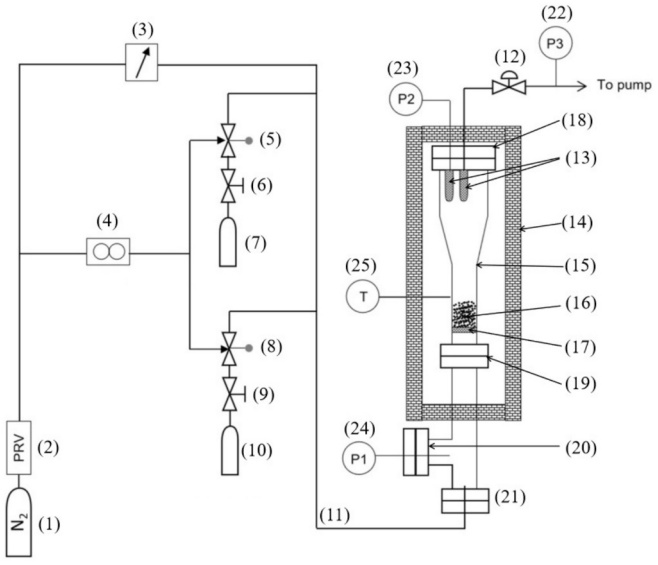

Fig. 1. Schematic diagram of FBR-ALD. The system mainly consists of (1) nitrogen container, (2) pressure reduction valve, (3) rotameter, (4) mass flow controller, (5) ALD valve 1, (6) manual valve 1, (7) steel bottle for precursor 1, (8) ALD valve 2, (9) manual valve 2, (10) steel bottle for precursor 2, (11) connecting pipelines, (12) diaphragm valve, (13) cylinder filter, (14) furnace, (15) reactor, (16) particle bed, (17) plate filter, (18–21) conflat flanges, (22) Pirani manometer P3, (23) Pirani manometer P2, (24) Pirani manometer P1, and (25) thermal couple.

2.2. Preparation process

CeO_2 nanoparticles (purity > 99.5 %) with particle size in the range of 20–50 nm were purchased from Shanghai Macklin Biochemical Co. Ltd. The color of the pristine CeO_2 nanoparticles displayed light yellow. The surface area of the nanoparticles was 36. 2 m^2/g measured by BET method. To fluidize the CeO_2 nanoparticles, nitrogen (N_2) gas was continuously introduced into the reaction vessel and the gas flow was depended on the particle mass. In this paper, the mass of CeO_2 nanoparticles was ~ 2.0 g and the flow of fluidizing gas was set at 0.1–0.4 L/min. For Al_2O_3 ALD process, Trimethylaluminium ($Al(CH_3)_3$, TMA) and deionized water (H_2O) were used as precursors. The reactor was set at the temperature of 177 ℃ and maintained at least 2 h with a continuous fluidizing gas before starting the ALD process. In one Al_2O_3 coating cycle, TMA and H_2O were introduced through multiple pulses and purges. The total dosing/purging times were 10 s/26.75 min for TMA pulses, and those were 5 s/14.25 min for H_2O pulses. The N_2 carrier gas of TMA and H_2O was set as 10 sccm. Both the containers of TMA and H_2O were set at room temperature. Regarding ALD ZnO process, diethylzinc ($Zn(C_2H_5)_2$, DEZ) and H_2O were selected as precursors. The reactor was heated to the reaction temperatures for at least 2 h with a continuous fluidizing gas before starting pulses of precursors. In one ZnO coating cycle, the dose manner of DEZ and H_2O was similar as TMA and H_2O. The total dosing/purging times of DEZ and H_2O were 6 s/17.75 min and 3 s/10.25 min, respectively. The N_2 carrier gas of DEZ and H_2O was set as 10 sccm. The containers of DEZ and H_2O were set at room temperature.

2.3. Characterization

Powder X-ray diffraction (XRD) results were obtained on Bruker D8 Advance with Cu-K_α radiation at $\lambda = 0.15418$ nm to analyze the phases of samples. The morphology and energy-disersive X-ray spectroscopy (EDX) of the ALD-coated nanoparticles were characterized by transmission electron microscopy (TEM, JEOL JEM F200) at 200 kV. The chemical states of surface elements were investigated by X-ray photoelectron spectroscopy (XPS, Thermo Scientific Nexsa G2) using monochromatic Al K_α X-ray source ($h\nu$ = 1486.6 eV), with the X-ray gun oriented at 30° to the horizontal plane. For XPS analysis of particle samples, the material was uniformly dispersed on double-sided conductive copper tape mounted on aluminum foil. To minimize charging effects, the sample surface was gently pressed to ensure good electrical contact and removed loose particles. The pass energies for survey and high-resolution XPS scans were set to 100 eV and 50 eV, respectively. All the survey and high-resolution XPS spectra were charge-corrected by referencing the C 1 s peak to 284.8 eV. The diffuse reflectance spectra (DRS) in the wavelength range of 250–1800 nm were collected by UV–vis–NIR spectrophotometer (PerkinElmer Lambda 1050 +), during which $BaSO_4$ was served as the reference. The Tauc plot method was employed to analyze the DRS results. The valence band-XPS (VB-XPS) was used to analyzed the valence band of the functionalized nanoparticles. The above-mentioned experiments can be illustrated using a process flow chart, as shown in Fig. 2.

3. Results and discussion

3.1. Amorphous Al_2O_3 coating

Different Al_2O_3 ALD cycles (0, 5, 10, and 20 cycles) were conducted on CeO_2 nanoparticles. Fig. 3 reveals that the pristine and ALD-coated CeO_2 nanoparticles show almost the same XRD patterns. The diffraction peaks (2θ) at 28.33°, 32.95°, 47.39°, 56.25°, 59.04°, 69.31°, 76.64°, 78.94°, and 88.36° correspond to the crystal planes (1 1 1), (2 0 0), (2 2 0), (3 1 1), (2 2 2), (4 0 0), (3 3 1), (4 2 0), and (4 2 2) of the cubic CeO_2 phase (PDF#34-0394), respectively. No Al_2O_3 peak is detected in the XRD patterns. It indicates that ALD-deposited Al_2O_3 films may be amorphous.

To investigate the influence of ALD coating on micro-strain and crystalline size of CeO_2 nanoparticles, the W-H (Williamson-Hall) method was employed, which can be expressed [42,43]:

$$\beta\cos\theta = \frac{K\lambda}{D} + 4\varepsilon \bullet \sin\theta \quad (1)$$

where β is the full width at half maxima (FWHM) of peaks, K represents the Scherrer constant (=0.9), λ is the wavelength of Cu-K_α radiation, D is the grain size, ε denotes the micro-strain, and θ is the angular position of

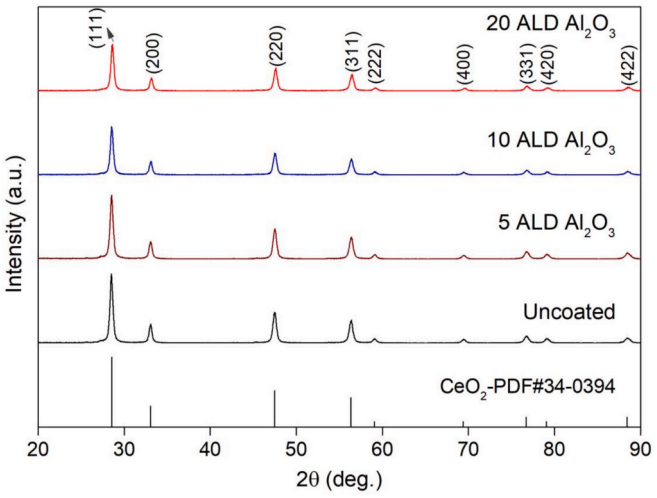

Fig. 3. XRD patterns of uncoated and Al_2O_3-coated CeO_2 nanoparticles with 0, 5, 10, and 20 ALD cycles.

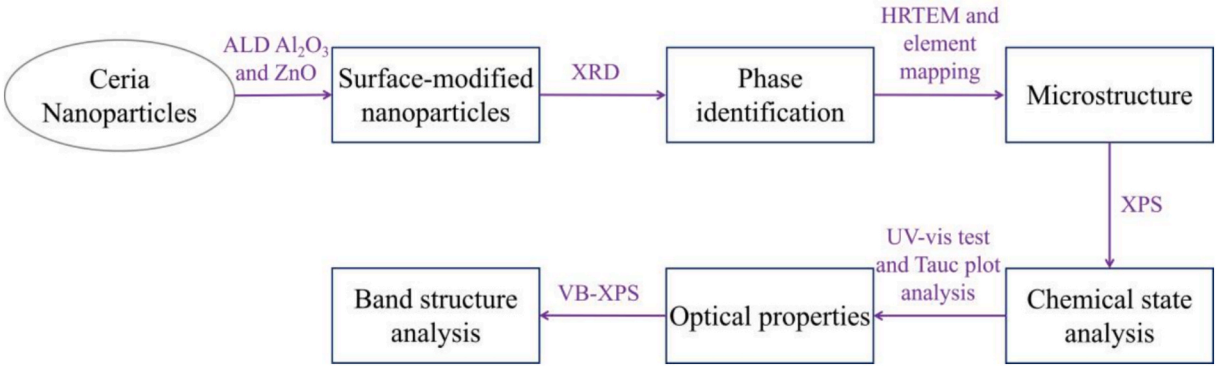

Fig. 2. Process flow chart of experiments.

XRD peaks (in radian). According to the W-H method described in references [44–46], the crystalline size is calculated from the intercept of the linear fitting the plot between βcosθ versus 4sinθ, and the slop of the plot represents the micro-strain. Due to the shapes of peaks, the FWHM of XRD peaks has been determined by fitting of Lorentz distribution of the 5 strongest peaks in the XRD patterns. The results of W-H plots are shown in Fig. S2 (Supporting Information). Based on the plots, the size and micro-strain of the ALD-modified CeO_2 nanoparticles are summarized in Table 1. The average crystalline size is 25–27 nm, showing no big difference, which can be ascribed to the ultrathin Al_2O_3 coating. On the other hand, the micro-strain first decreases slowly and then increases slightly. The low micro-strain of 5 ALD Al_2O_3 samples may be attributed to the high deposition temperature of 177 ℃ and non-uniform Al_2O_3 coatings onto CeO_2 nanoparticles caused by nucleation delay in ALD Al_2O_3 process. As the number of Al_2O_3 ALD increases beyond 10, the uniform coating could impose strain on the CeO_2 nanoparticles, thereby inducing increase of micro-strain.

To investigate the morphology of Al_2O_3 films, TEM analysis was conducted. Fig. 4a clearly shows that the surfaces of nanoscale CeO_2 are clean and no coating is found on the nanoparticles. As the number of ALD cycles increases to 10, a nanoscale film is obviously found on the CeO_2 nanoparticles as a shell (Fig. 4b) and the coated film seems to be thicker in the samples with 20 ALD cycles (Fig. 4c). The morphological analysis confirms that ultrathin, conformal Al_2O_3 films are successfully coated onto CeO_2 nanoparticles via a homemade FBR-ALD system, resulting in a core@shell structure.

For uncoated CeO_2, the HRTEM images clearly show that the same lattice fringes exist both on the surfaces and inside the nanoparticles, as shown in Figs. 5a and d. The spacing distance of 0.282 nm marked in Fig. 5d represents crystal plane (2 0 0) of CeO_2 with cubic phase. As the number of ALD cycles increases to 10, a nanoscale film with a thickness of about 1.9 nm is observed to cover the CeO_2 nanoparticle as a shell, forming a CeO_2@Al_2O_3 core@shell structure (Fig. 5b). Meantime, no lattice fringe is seen in the coated nanofilms, as indicated by the white dashed line enclosed area (Fig. 5e). When the number of ALD cycles increases further to 20, the coated nanofilms become thicker to ca. 3.8 nm (Fig. 5c). The morphology of the coated nanofilms shows no lattice fringe while the lattice fringe with a spacing distance of 0.328 nm represents crystal plane (1 1 1) of CeO_2 (Fig. 5f). HRTEM analysis evidently verifies that the ALD-coated Al_2O_3 nanofilms on CeO_2 nanoparticles are amorphous. It has been reported that the growth rate of Al_2O_3 nanofilms on ZrO_2 nanoparticles can reach ca. 0.2 nm/cycle [33]. Our growth rate of Al_2O_3 of ca. 0.19 nm/cycle agrees with the reported result. From the EDX mapping of the CeO_2 nanoparticle deposited with 10 ALD Al_2O_3 cycles, a nanoscale shell with the thickness of ca. 1.9 nm, which is rich in Al and O elements and poor in Ce element, is observed in the outer surface of CeO_2, as shown in Fig. 5g–l. The EDX results further confirm that the ALD-coated Al_2O_3 nanofilms on CeO_2 nanoparticles using TMA and H_2O as precursors at 177 °C are amorphous alumina oxide.

XPS spectra of Al_2O_3-coated CeO_2 nanoparticles were recorded to investigate the chemical states of surface elements, as the results shown in Fig. 6. The survey spectra of uncoated and Al_2O_3-coated CeO_2 nanoparticles with 5 and 10 ALD cycles are shown in Fig. 6a. It is clearly seen that peaks with binding energies of ca. 74.1 eV appear in the Al_2O_3-coated samples. These peaks belong to Al 2p of the coated amorphous Al_2O_3, which are also confirmed in the Al 2p high-resolution XPS spectra (Fig. 6b). In uncoated and Al_2O_3-coated CeO_2 nanoparticles, the high-resolution XPS spectra of Ce 3d and O 1 s are shown in Figs. 6c and d, respectively. Fig. 6c displays the fitted peaks of Ce 3d high-resolution XPS spectra and the results agree well with the ref. [47,48]. The peaks marked as v, v″, v‴, u, u″, and u‴ with binding energies of ca. 881.8 eV, 888.3–888.4 eV, 897.7 eV, 900.4 eV, 906.9–907.0 eV, and 916.1 eV, respectively, belong to Ce^{4+} ion, while v^0, v′, u^0, and u′ with binding energies of ca. 879.8–880.0 eV, 884.2–884.4 eV, 897.6–898.2 eV, and 903.1 eV, respectively, belong to Ce^{3+} ion. All the Ce 3d XPS results of binding energies and FWHM are listed in Table S1 (Supporting Information). The peak fitting parameters, i.e., FWHM, are consistent with the references [49,50]. The existence of Ce^{3+} ion in CeO_2 nanoparticles is caused by oxygen vacancies, which is a common defect in oxide nanoparticles [51]. As the number of Al_2O_3 ALD cycles increases, the profiles of high-resolution XPS of O 1 s become distinct. Fig. 6d displays the peak fitting of O 1 s high-resolution XPS spectra. For the uncoated CeO_2 sample, the binding energies of 529.0 eV and 531.2 eV belong to the lattice oxygen (O-M-O) and oxygen vacancy (V_O), respectively, while those of lattice oxygen and oxygen vacancy remain almost the same in Al_2O_3-coated CeO_2 nanoparticles. However, the relative percentages of these two states of O 1 s are different. As summarized in Table 2, the percentage of lattice oxygen decreases from 72.7 % in uncoated CeO_2 nanoparticles to 11.4 % in 10 ALD Al_2O_3-coated counterparts while the oxygen vacancy increases from 27.3 % in uncoated samples to 88.6 % in 10 ALD Al_2O_3-coated ones. Additionally, the ratio of atomic percentage of V_O/O-M-O increases from 0.37 to 7.77 drastically. It is worth noting that the ratio of atomic percentages between Ce^{3+} and Ce^{4+} in uncoated CeO_2 nanoparticles is calculated as 0.30, which agrees with the value of 0.37 obtained from O 1 s spectrum. In addition, the FWHM of oxygen vacancy enlarges from 2.1 eV to 3.0 eV, which can be attributed to the drastic increase of oxygen vacancy induced by amorphous Al_2O_3 coating. As the HRTEM results shown, the thickness of the Al_2O_3 nanofilm increases with the number of ALD cycles. It is worth noting that the results of XPS are the information about the surface of samples with the depth in the range of 1–10 nm. Therefore, the oxygen vacancies in Al_2O_3 nanofilms induce the increase of oxygen vacancies in the CeO_2@Al_2O_3 core@shell nanocomposites. On the other hand, the XPS results verify that the ALD-coated Al_2O_3 nanofilms on CeO_2 are amorphous and rich in oxygen vacancies.

Table 1
Crystalline size and micro-strain of Al_2O_3-modified CeO_2 nanoparitcles.

Physical parameter	Pristine sample	Different Al_2O_3 ALD cycles		
		5	10	20
Crystalline size (nm)	26.3	24.8	26.9	26.2
Micro-strain ($\times 10^{-3}$)	0.89	0.75	0.98	0.92

3.2. Crystalline ZnO coating

For depositing ZnO nanofilms on CeO_2 nanoparticles, different reactor temperatures (80 ℃, 100 ℃, 120 ℃, 150 ℃, and 177 ℃) and ALD cycles (0, 10, 20, and 30) were conducted in the homemade FBR-ALD system. Fig. 7 shows the XRD results of different CeO_2 nanoparticles with different coating conditions. At different reactor temperatures, CeO_2 with cubic structure (PDF#36-0394) is clearly detected in all the samples (Fig. 7a). As the reactor temperature increases from 80 ℃ to 177 ℃, XRD peaks of crystalline ZnO with wurtzite structure begin to appear. At 177 ℃, the diffraction peaks at 31.56° and 36.22°, which represent the crystal planes (1 0 0) and (1 0 1) of the wurtzite ZnO phase (PDF#36–1451), respectively, are more distinct than that of the samples deposited at 80 ℃ (Fig. 7b). As ZnO ALD cycles increase to 30 with the reactor temperature remaining at 177 ℃, the peaks (1 0 0) and (1 0 1) of crystalline ZnO appear more obvious than other samples, as shown in Figs. 7c and d. The XRD results indicate that it could improve the crystallinity of atomic layer-deposited ZnO on CeO_2 nanoparticles by appropriately increasing reactor temperature and the number of ALD cycles.

Similar to process the XRD data of Al_2O_3 ALD samples, the W-H plots were obtained to analyze the micro-strain and average size, as shown in Figs. S3 and S4 (Supporting Information). And the results of crystalline size and micro-strain are summarized in Table 3. It is noteworthy that the ZnO related peaks are not adequate in the XRD patterns and the W-H plots is based on the XRD peaks of CeO_2. The crystalline size shows no

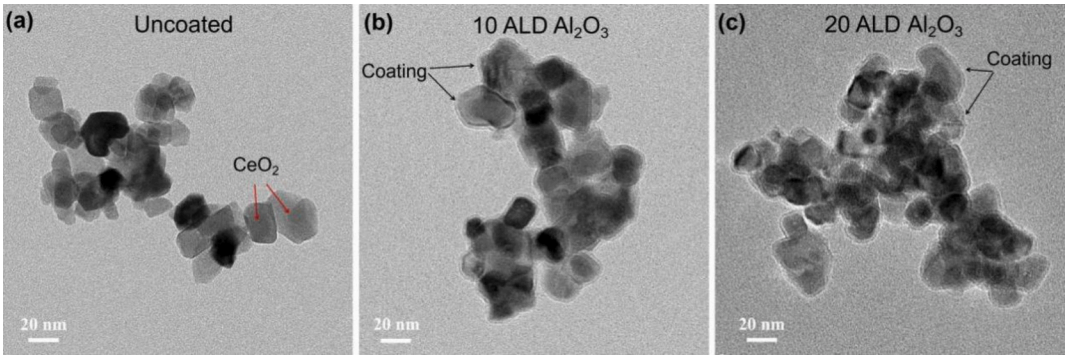

Fig. 4. TEM images of CeO_2 nanoparticles with different ALD Al_2O_3 cycles: (a) uncoated, (b) 10 ALD cycles, (c) 20 ALD cycles.

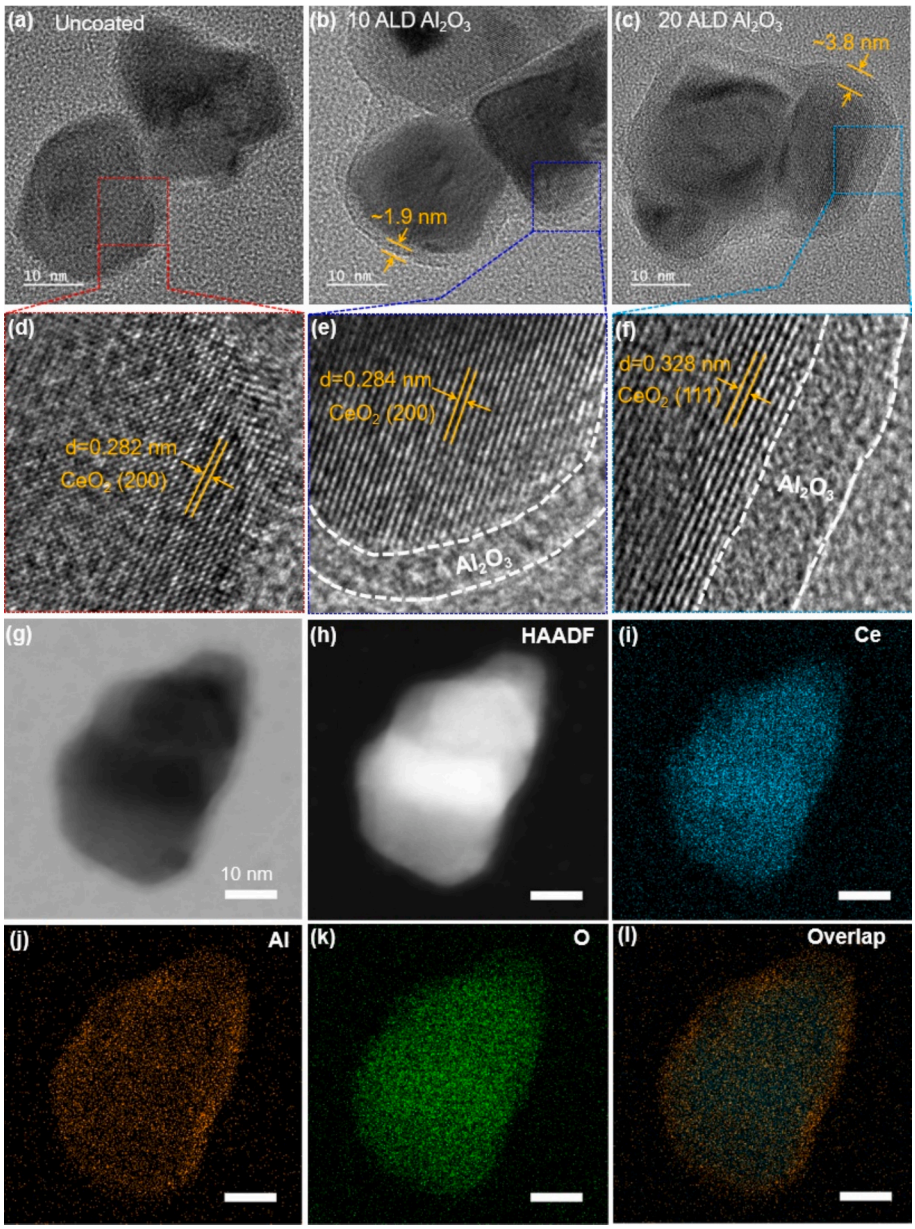

Fig. 5. HRTEM of CeO_2 nanoparticles for uncoated sample (a, d), 10 ALD Al_2O_3 sample (b, e), and 20 ALD Al_2O_3 sample (c, f). (g–l) STEM-EDX of Al_2O_3-coated CeO_2 nanoparticles with 10 ALD cycles.

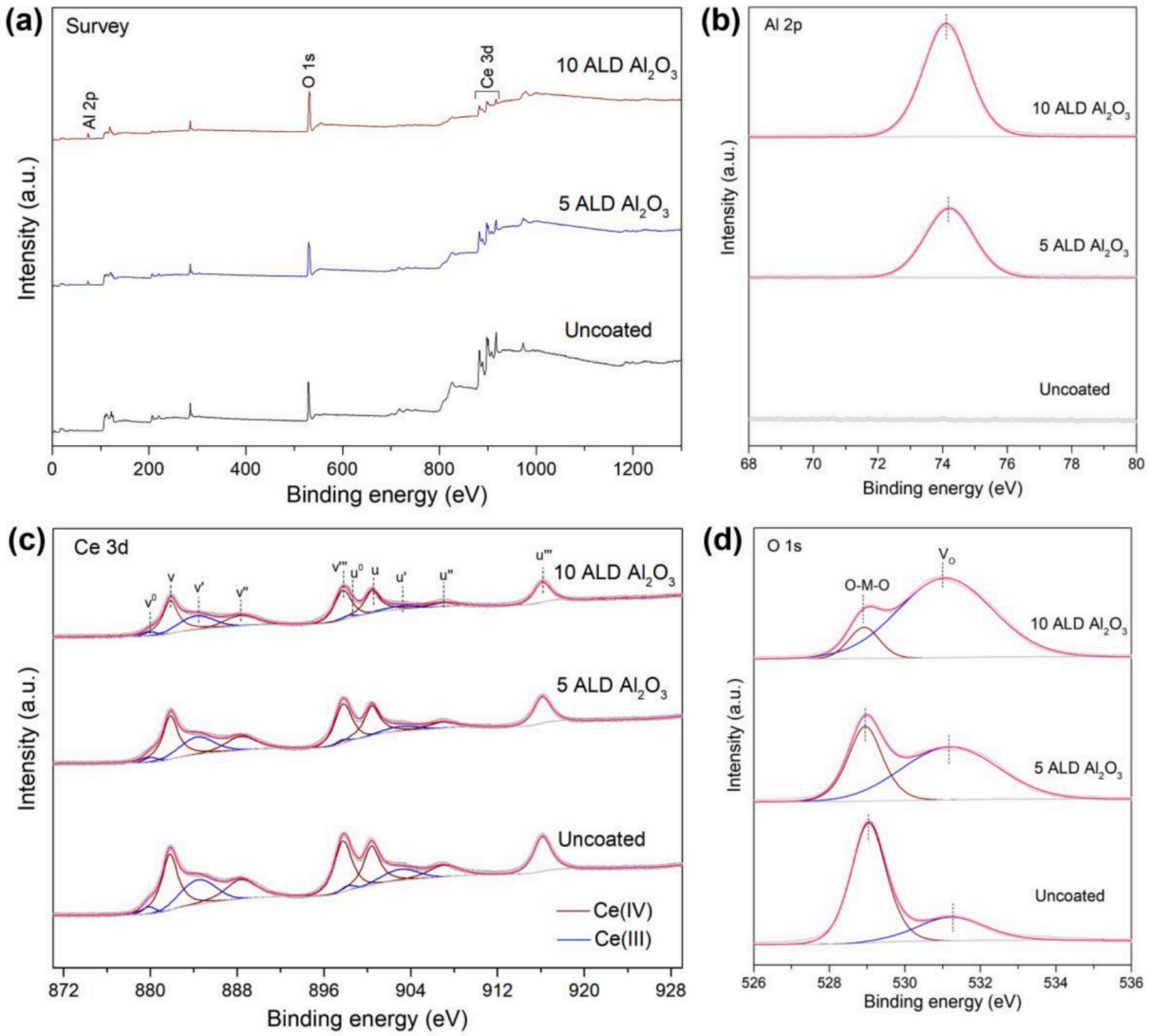

Fig. 6. (a) Total XPS spectra of uncoated and Al_2O_3-coated CeO_2 nanoparticles. (b) XPS spectra of Al 2p. (c) XPS spectra and peak fitting of Ce 3d. (d) XPS spectra and peak fitting of O 1 s.

Table 2
XPS results for the uncoated and Al_2O_3-coated CeO_2 nanoparticles: binding energies (eV); (FWHM *); relative percentages.

O 1 s	Binding energy (FWHM) Relative percentage		
	Uncoated	5 ALD Al_2O_3	10 ALD Al_2O_3
O–Ce–O	529.0 (1.1) 72.7 %	528.9 (1.1) 34.8 %	528.9 (1.0) 11.4 %
V_O	531.2 (2.1) 27.3 %	531.2 (3.0) 65.2 %	531.1 (3.0) 88.6 %

* full width at half maxima, (eV).

big difference after ZnO ALD with different deposition temperatures and number of ALD cycles. Before 100 ℃, the micro-strain of CeO_2 initially increases slightly, then decreases and remains stable up to 177 ℃. It indicates that high crystallinity of ZnO coatings could reduce the micro-strain in CeO_2 nanoparticles. As the number of ZnO ALD cycles increases, the micro-strain increases slightly, which can be attributed to the increased thickness of ZnO coatings.

Fig. 8 shows the morphology of ZnO-coated CeO_2 nanoparticles. For the sample with 10 ALD ZnO@80 ℃, non-conformal coatings are seen on CeO_2 (Fig. 8a) while lattice fringes are clearly displayed in the non-conformal coating (Figs. S5a–b in Supporting Information). It indicates that crystalline ZnO is formed in the atomic-layer-deposited nanofilms at that temperature. As the temperature increases to 177 ℃, more conformal coating is found on the CeO_2 nanoparticle (Fig. S5c in Supporting Information) and the average thickness can be found ca. 2.5 nm (Fig. 8b). Further increasing the number of ALD cycle to 30, thicker ZnO coating (~7.5 nm) is found on the CeO_2 nanoparticle as a shell, thereby forming a CeO_2@ZnO core@shell structure (Fig. 8c). It has been reported that the growth rate of ZnO nanofilms on TiO_2 and SiO_2 nanoparticles is ca. 0.2 nm/cycle [52]. A growth rate of about 0.22 nm/cycle has been achieved for ZnO ALD coated onto multiwalled carbon nanotubes [53]. Our growth rate of ZnO ALD is similar to the reported results. Since that crystalline ZnO is deposited on CeO_2 nanoparticles, the interfaces between cubic CeO_2 and wurtzite ZnO could form heterostructures.

In order to clarify the CeO_2/ZnO interface, HRTEM was conducted for the sample with 30 ALD ZnO cycles deposited at 177 ℃. Fig. 9a–d show that CeO_2 core with crystal plane (1 1 1) is surrounded by a nanofilm coating with different lattice fringes, indicating polycrystallinity of deposited ZnO nanofilms. By zooming the areas enclosed by rectangles in Fig. 9a, marked as Site 1, Site 2, and Site 3, the results are shown in Fig. 9b–d. Site 1 can be divided into two parts by a white dashed line, showing different patterns of lattice fringes (Fig. 9b). The spacing distance of 0.265 nm represents the crystal plane (002) of crystalline ZnO with wurtzite structure while other part represents

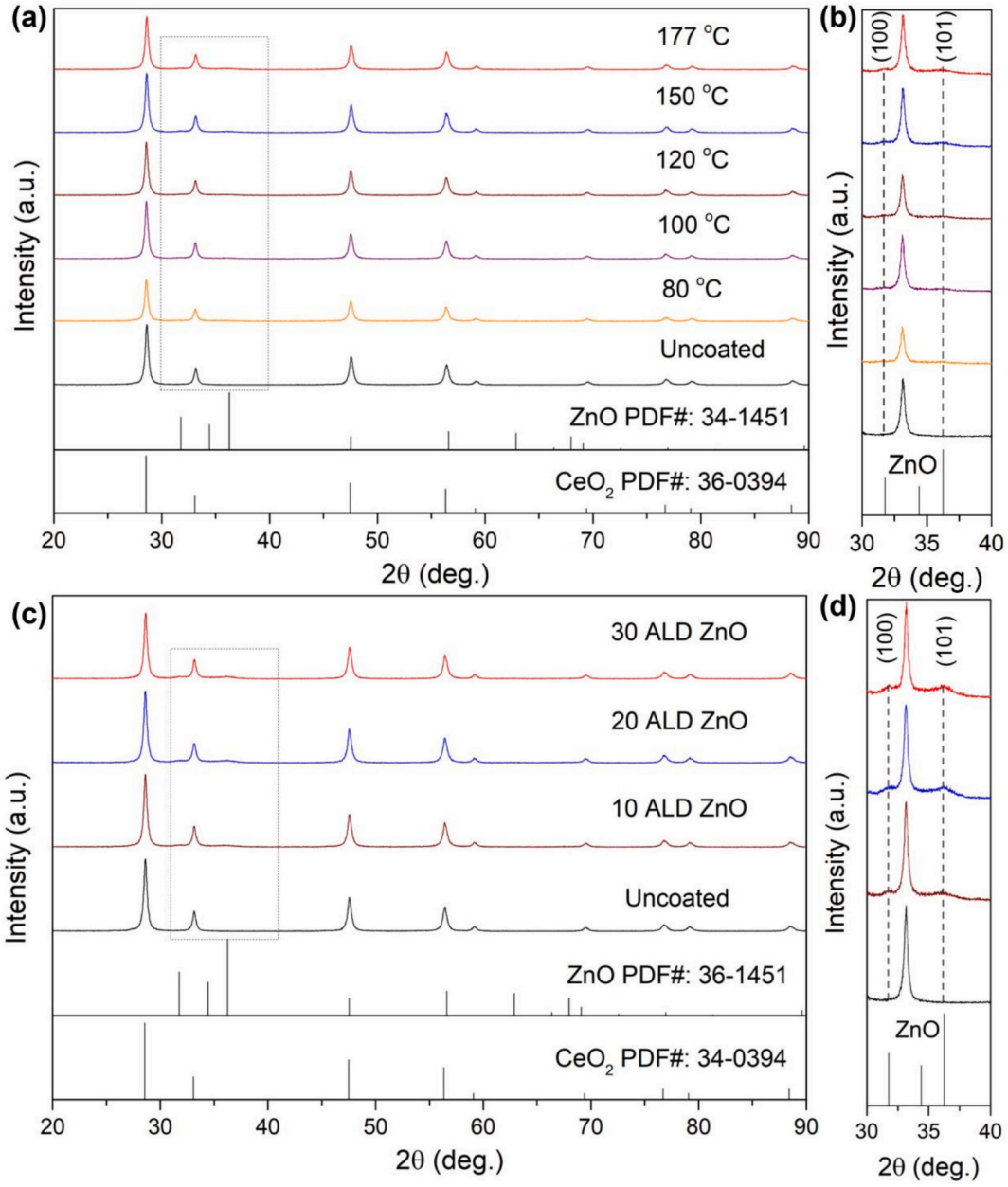

Fig. 7. XRD patterns of uncoated and ZnO-coated CeO_2 nanoparticles. (a–b) 10 ZnO ALD cycles at different temperatures. (c–d) Different ALD cycles with reactor temperature at 177 ℃.

Table 3
Crystalline size and micro-strain of ZnO-modified CeO_2 nanoparticles.

Physical parameter	Pristine sample	Different temperature (℃) with 10 ALD cycles					Different ALD cycles at 177 ℃	
		80	100	120	150	177	20	30
Crystalline size (nm)	26.3	28.41	28.89	27.46	26.46	25.97	25.97	26.72
Micro-strain ($\times 10^{-3}$)	0.89	0.92	0.96	0.75	0.79	0.78	0.65	0.79

crystal plane (1 1 1) of cubic CeO_2. Thus, the white dashed line is the interface between these two phases. Similar interfaces are found in Site 2 and Site 3 (Figs. 9c and d). The HRTEM analysis demonstrates that CeO_2/ZnO heterostructures are formed in ZnO-coated CeO_2 nanoparticles. STEM-EDX mapping of the sample shows that a nanoscale shell, rich in Zn and O elements, is on the outer of the CeO_2 core (Fig. 9e–j), which further confirms that CeO_2 is enclosed by a polycrystalline ZnO film with a nanoscale thickness.

XPS spectra are also used to analyze the chemical states of surface elements in ZnO-coated CeO_2 nanoparticles. The survey spectra of uncoated and ZnO-coated CeO_2 nanoparticles with different ALD cycles and different reactor temperatures are shown in Fig. 10a. Compared to uncoated CeO_2 sample, the ZnO-coated CeO_2 nanoparticles clearly show Zn 2p peaks and other peaks such as Zn 3d, Zn 3p, Zn 3 s, Zn(LMM), and Zn 2 s. To verify the chemical states in ZnO-coated CeO_2 samples, the XPS of ZnO nanoparticles with the purity of 99.9 % and the diameter in

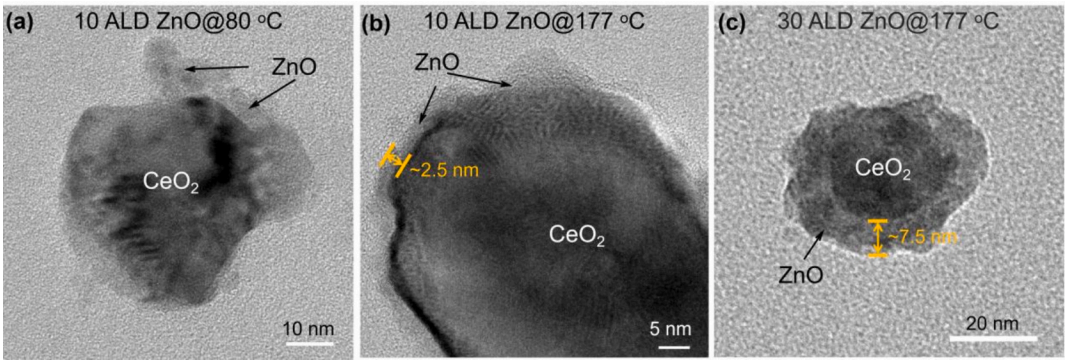

Fig. 8. TEM images of uncoated and ZnO-coated CeO_2 nanoparticles. (a) Sample with 10 ALD cycles deposited at 80 °C. (b) Sample with 10 ALD cycles deposited at 177 °C. (c) Sample with 30 ALD cycles deposited at 177 °C.

the range of 20–40 nm has been conducted, as the results shown in Fig. S6 (Supporting Information). The Zn-related peaks observed in ZnO-coated CeO_2 nanoparticles (Fig. 10a) agree well with those in the ZnO survey spectrum (Fig. S6a in Supporting Information). High-resolution XPS of Zn 2p further confirms that Zn 2p with binding energies at 1021.5 eV (Zn 2p3/2) and 1044.6 eV (Zn 2p1/2) exists in the ZnO-coated CeO_2 nanoparticles, as shown in Fig. 10b. In uncoated and ZnO-coated CeO_2 nanoparticles, the high-resolution XPS spectra of Ce 3d and O 1 s are shown in Figs. 10c and d. Fig. 10c displays the peak fitting of Ce 3d high-resolution XPS spectra. The peaks, marked as v, v″, v‴, u, u″, and u‴ with binding energies of 881.8–881.9 eV, 888.2–888.4 eV, 897.6–897.8 eV, 900.2–900.4 eV, 907.0–907.1 eV, and 916.0–916.1 eV, respectively, belong to Ce^{4+} ion, while v^0, v′, u^0, and u′ with binding energy of 880.0–880.7 eV, 883.7–884.3 eV, 898.3–898.4 eV, and 902.6–903.1 eV, respectively, belong to Ce^{3+} ion. The peak fitting parameters regarding Ce 3d for ZnO-coated CeO_2 nanoparticles, i.e., FWHM, are listed in Table S2 (Supporting Information). Compared to the uncoated CeO_2, the high-resolution XPS spectra of O 1 s for ZnO-coated CeO_2 nanoparticles become distinct, and the difference appears more obvious for the sample with 30 ALD cycles. Fig. 10d shows the results of peak fitting for the high-resolution XPS spectra of O 1 s. From the O 1 s spectra of the uncoated CeO_2 sample, there are two binding energies of 531.2 eV (V_O) and 529.0 eV (O–Ce–O). Compared to the uncoated CeO_2 nanoparticles, three peaks of O 1 s located at 528.8–529.0 eV, 530.1–530.3 eV, and 531.7–531.8 eV, are obviously found in the ZnO-coated CeO_2 sample, as displayed in Fig. 10d. For ZnO nanoparticles, the binding energies of O–Zn–O and V_O are located at 530.2 eV and 531.8 eV, respectively (Fig. S6b in Supporting Information). Based on the analysis of O 1 s XPS in ALD-coated CeO_2 and ZnO nanoparticles, it can be concluded that the binding energies located at 530.1–530.3 eV and 528.8–529.0 eV belong to the lattice oxygen, namely O–Zn–O and O–Ce–O, respectively. And the binding energy located at 531.7–531.8 eV belongs to oxygen vacancies. Thus, in ZnO-coated CeO_2 nanoparticles, there are two types of lattice oxygen (O–Ce–O and O–Zn–O) and one oxygen vacancy (V_O). The binding energy and related percentage of O 1 s for ZnO-coated CeO_2 nanoparticles are summarized in Table 4. For all the uncoated and ZnO-coated CeO_2 samples, the binding energies of lattice oxygen O–Ce–O remain constant at ca. 529.0 eV. However, the relative percentage decreases steadily from 72.7 % for uncoated samples to 11.6 % for 30 ALD ZnO@177 °C sample. The binding energy of O–Zn–O lattice oxygen for the ZnO-coated CeO_2 sample stands at 530.1–530.3 eV, agreeing well with the binding energy of 530.2 eV for pure ZnO nanoparticles. And the relative percentage of O–Zn–O increases from 28.2 % for 10 ALD ZnO@80 °C sample to 62.2 % for 30 ALD ZnO@177 °C sample. The binding energy of V_O in the uncoated CeO_2 sample is 531.2 eV, smaller than that of V_O 531.9 eV in pure ZnO nanoparticles. In the ZnO-coated CeO_2 sample, the binding energy of V_O is in the range of 531.7–531.8 eV, higher than that in the uncoated CeO_2 sample (531.2 eV). The relative percentage of V_O decreases from 33.0 % for 10 ALD ZnO@80 °C samples to 28.2 % for 10 ALD ZnO@177 °C samples, and further reduces to 26.2 % for 30 ALD ZnO@177 °C samples. It is worth noting that the relative percentage of oxygen vacancy V_O is 33.3 % in ZnO nanoparticles. The relative percentage of low content of oxygen vacancies and high content of lattice oxygen indicate high crystallinity of ZnO nanofilms in the 30 ALD ZnO@177 °C samples, which agrees with the XRD results. Additionally, the FWHM of oxygen vacancies is about 1.7–1.8 eV for ZnO-coated samples, which is much lower than that for Al_2O_3-coated samples (ca. 3.0 eV) with amorphous coatings. From the ratio of relative percentage of O 1 s in ZnO-coated CeO_2 samples (Table 5), O–Zn–O/O–Ce–O increases from 0.73 for the 10 ALD ZnO@80 °C sample to 5.36 for the 30 ALD ZnO@177 °C sample. Meantime, V_O/O–Ce–O increases from 0.85 for the 10 ALD ZnO@80 °C sample to 2.25 for the 30 ALD ZnO@177 °C sample. The relative high percentage of O–Zn–O for samples ZnO ALD deposited at 177 °C indicates that the crystallinity of ZnO nanofilms could be improved by increasing reactor temperature. And the highest ratio of lattice oxygen O–Zn–O in the 30 ALD ZnO sample is attributed to the thicker crystalline ZnO nanofilms.

3.3. *UV-blocking property*

To investigate the optical absorption properties of the uncoated and ALD-coated CeO_2 nanoparticles, DRS were conducted on a UV–vis-NIR spectrometer. For Al_2O_3-coated nanoparticles, the DRS in the range of 250–800 nm show an intense absorption of UV light (Fig. 11a). As the number of ALD cycles increases, the reflectance in the visible light (400–800 nm) decreases. With Al_2O_3 coating on CeO_2 nanoparticles, the appearance of powders change from light yellow to light gray and becomes further gray as the number of ALD cycles increases (the inset of Fig. 11a). On the other hand, after 10-cycle Al_2O_3 ALD, the UV-absorption edge exhibits a blue shift, showing decreased value of the absorption edge.

Regarding ZnO-coated samples, at different reactor temperatures, the DRS in the range of 250–800 nm show an intense absorption of UV light, and UV-absorption edge appears a slight red shift as the reactor temperature increases. Specifically, the CeO_2 samples deposited at 177 °C has the largest UV-absorption edge of ca. 377 nm compared to that of 371 nm for uncoated CeO_2 samples (Figs. S7a and b in Supporting Information). For the samples deposited at 177 °C with different ALD cycles, the DRS results are illustrated in Fig. 11c. From the figure, the DRS spectra in the range of 250–800 nm show an intense absorption of UV light, similar to that of Al_2O_3-coated CeO_2 nanoparticles. As the number of ZnO ALD cycles increases, the reflectance in the visible light (400–800 nm) decreases. And the color of powders changes from light yellow to light gray (the inset of Fig. 11c). Moreover, with an increase of the number of ZnO ALD cycles, a red shift of the UV-absorption edge occurs, differing from that of Al_2O_3-coated samples.

To further investigate the color of appearance of powders in the

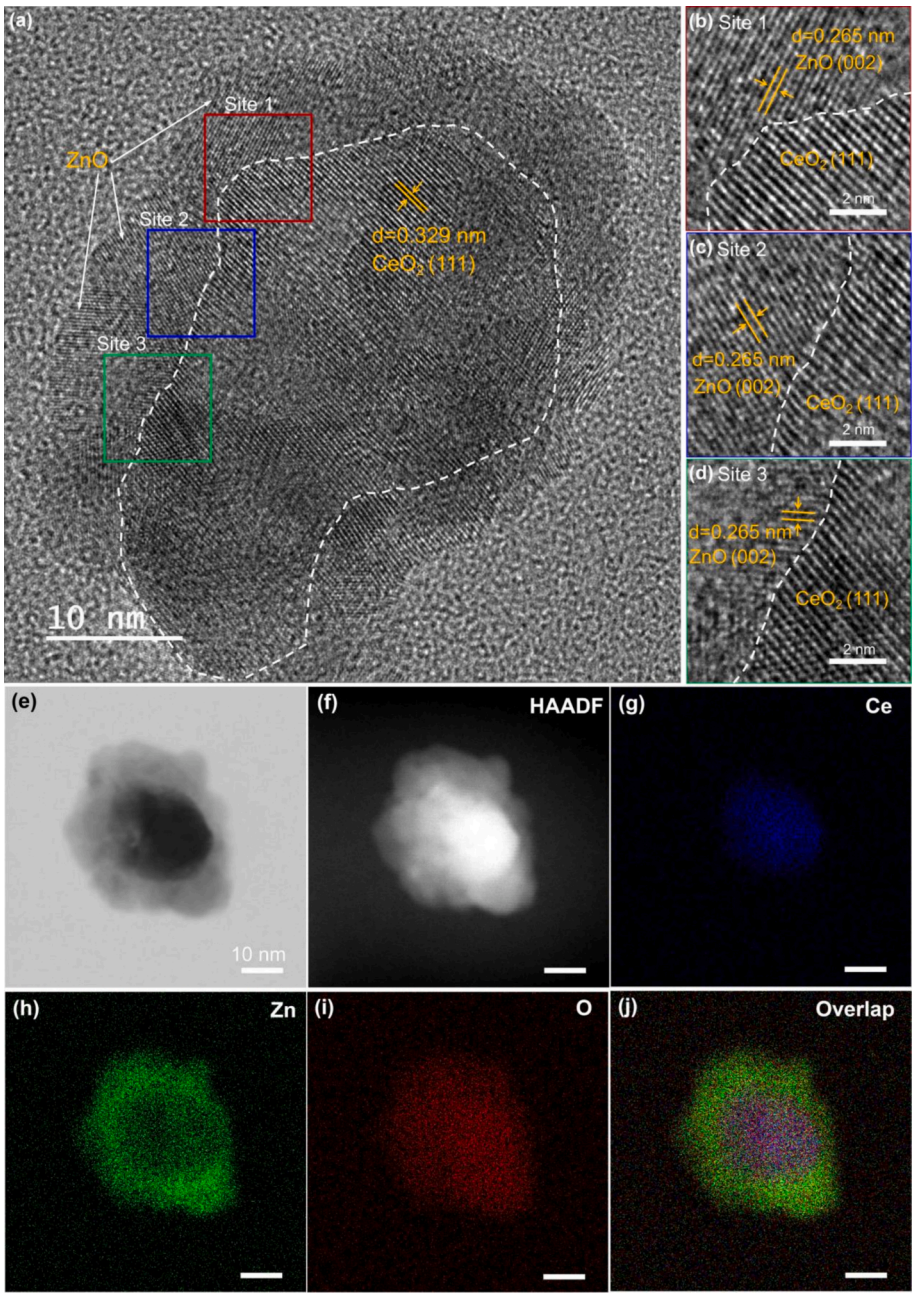

Fig. 9. (a) HRTEM of ZnO-coated CeO_2 nanoparticles with 30 ALD cycles at 177 ℃. (b), (c), and (d) Enlarged images of areas marked as Site 1, Site 2, and Site 3 in (a), respectively. (e–j) STEM-EDX mapping of ZnO-coated CeO_2 nanoparticles with 30 ALD cycles at 177 ℃.

visible light, the average reflectance $\overline{R}$ is defined as follows:

$$\overline{R} = \frac{\int_{\lambda_1}^{\lambda_2} R \bullet \mathrm{d}\lambda}{(\lambda_2 - \lambda_1)} \tag{2}$$

where λ_1 and λ_2 represent the wavelength, and R is the measured reflectance. Based on the equation, the average reflectance of the samples in the wavelength range of 400–800 nm is calculated and displayed in Figs. 11b and d. For the pristine CeO_2 nanoparticles, the reflectance in the ranges of 570–600 nm (yellow light region) is larger than those in 400–500 nm (blue light region) and 500–570 nm (green light region), resulting light yellow color for uncoated CeO_2 nanoparticles. As Al_2O_3 and ZnO coating on CeO_2 nanoparticles, the average reflectance in the different wavelength regions decreases. However, the reflectance in the yellow light region drops faster than that in the blue light region and green light region, resulting the latter outperforming the former. As the number of ALD cycles increases beyond 10 for Al_2O_3-coated samples and 20 for ZnO-coated samples, the color of coated CeO_2 nanoparticles becomes light gray or even medium gray. It indicates that the thickness of ALD-coated nanofilms affects the appearance of CeO_2 nanoparticles. Additionally, the thicker coatings can lead to the disappearance of absorption in the NIR region for CeO_2 nanoparticles. In the uncoated CeO_2 samples, a weak absorption occurs between 1360 and 1455 nm, which disappears both in Al_2O_3-coated samples with beyond 10 ALD cycles and ZnO-coated samples with beyond 10 ALD cycles (Figs. S8a and b in Supporting Information).

For the UV-absorption edge shifting in the ALD-coated samples, Fig. 11e clearly shows the difference of UV-absorption edges in the range of 300–500 nm. The optical band-gap energies can be analyzed by Tauc's equation [54–56]:

$$(\alpha h\nu)^{1/n} = A(h\nu - E_g) \tag{3}$$

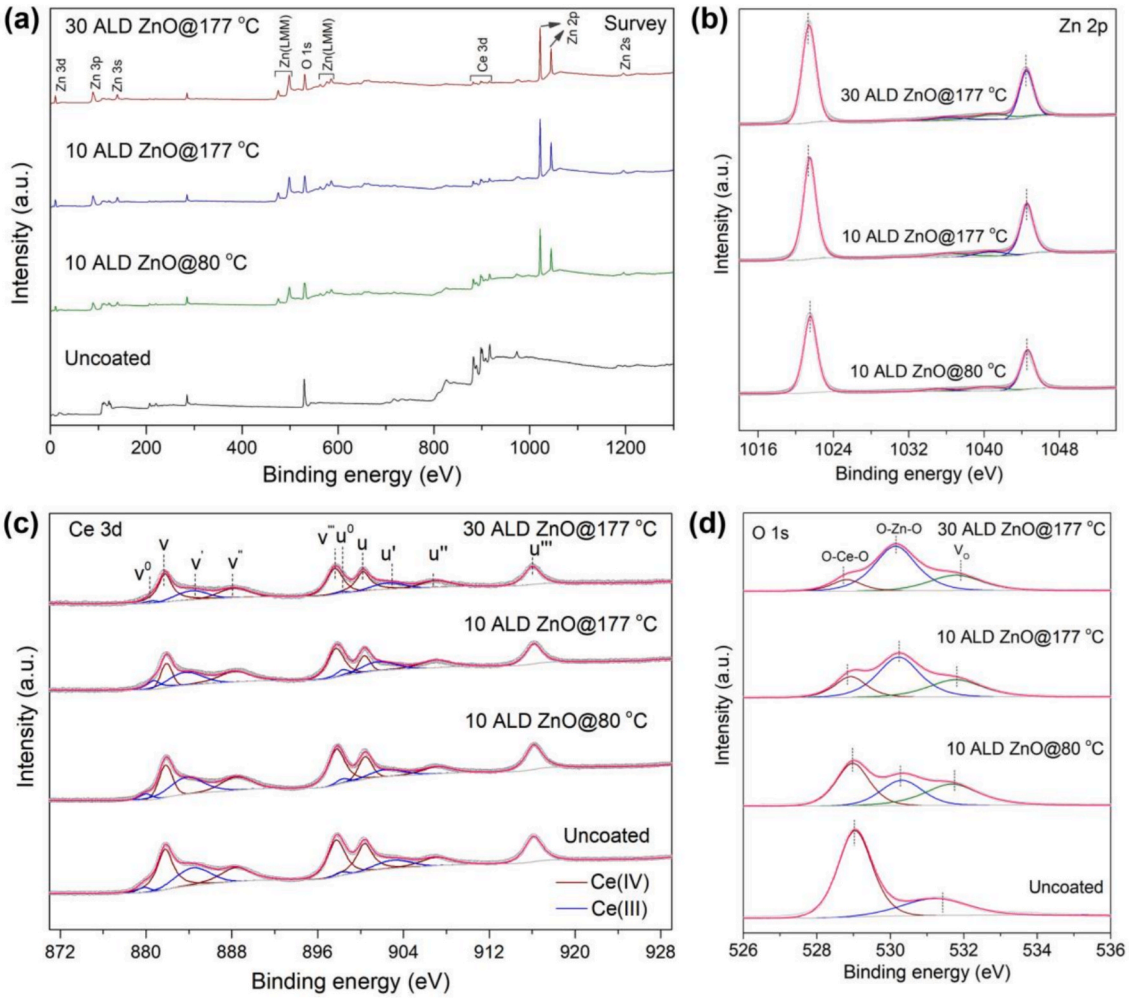

Fig. 10. (a) Total XPS spectra of uncoated and ZnO-coated CeO_2 nanoparticles. (b) XPS spectra of Zn 2p. (c) XPS spectra and peak fitting of Ce 3d. (d) XPS spectra and peak fitting of O 1 s.

Table 4
XPS results for the ZnO-coated CeO_2 nanoparticles: binding energies (eV); (FWHM); relative percentages.

O 1 s	Binding energy (FWHM) Relative percentage				
	Uncoated	Pure ZnO	10 ALD@80 ℃	10 ALD@177 ℃	30 ALD@177 ℃
O–Ce–O	529.0 (1.1) 72.7%	–	529.0 (1.1) 38.8 %	528.9 (1.0) 20.2 %	528.8 (1.0) 11.6 %
O–Zn–O	–	530.2 (1.3) 66.7 %	530.3 (1.3) 28.2 %	530.2 (1.4) 51.6 %	530.1 (1.4) 62.2 %
V_O	531.2 (2.1) 27.3 %	531.8 (1.9) 33.3 %	531.7 (1.8) 33.0 %	531.8 (1.7) 28.2 %	531.8 (1.7) 26.2 %

Table 5
Ratio of relative percentage in ZnO-coated CeO_2 nanoparticles.

O 1 s	Ratio of relative percentage			
	Uncoated	10 ALD@80 ℃	10 ALD@177 ℃	30 ALD@177 ℃
O–Zn–O/ O–Ce–O	0	0.73	2.55	5.36
V_O/O–Ce–O	0.37	0.85	1.40	2.25

where α is the absorption coefficient, $h\nu$ is the photon energy (eV), A is a physical constant related to the material, E_g is the band-gap energy (eV), and n characterizes the electronic transition type of the materials (n = 1/2 for direct band-gap materials; n = 2 for indirect band-gap materials). In this study, the band-gap energies of the uncoated, 10 ALD Al_2O_3, and 30 ALD ZnO samples are determined through Tauc plot analysis for direct band-gap materials (n = 1/2). To analyze the DRS data obtained from the particle samples, the Kubelka-Munk function $F(R)$ was employed, which is expressed as follows [57–59]:

$$F(R) = \frac{(1-R)^2}{2R} \tag{4}$$

where R ($0 < R < 1$) represents the measured reflectance of the samples. Assuming that the absorption coefficient (α) is proportional to the Kubelka-Munk function $F(R)$, the band-gap energies can be obtained from the plot of $[F(R)h\nu]^2$ versus $h\nu$, as the intercept of the extrapolated linear part of the plot at $[F(R)h\nu]^2 = 0$. Based on the UV–vis DRS, the corresponding curves are obtained and displayed in Fig. 11f. The band-gap energies of the uncoated, 10 ALD Al_2O_3-coated, and 30 ALD ZnO-coated CeO_2 nanoparticles are found to be 3.34, 3.39, and 3.21 eV, respectively. On the other hand, the reflectance onset wavelength obtained by extrapolation of the DRS curves shows comparable band-gap energies, which are found to be 3.33, 3.41, and 3.25 eV, as listed in Table 6. The results indicate that the ZnO coating lead to a decease of band-gap energy for CeO_2 nanoparticles while the Al_2O_3 coating gives

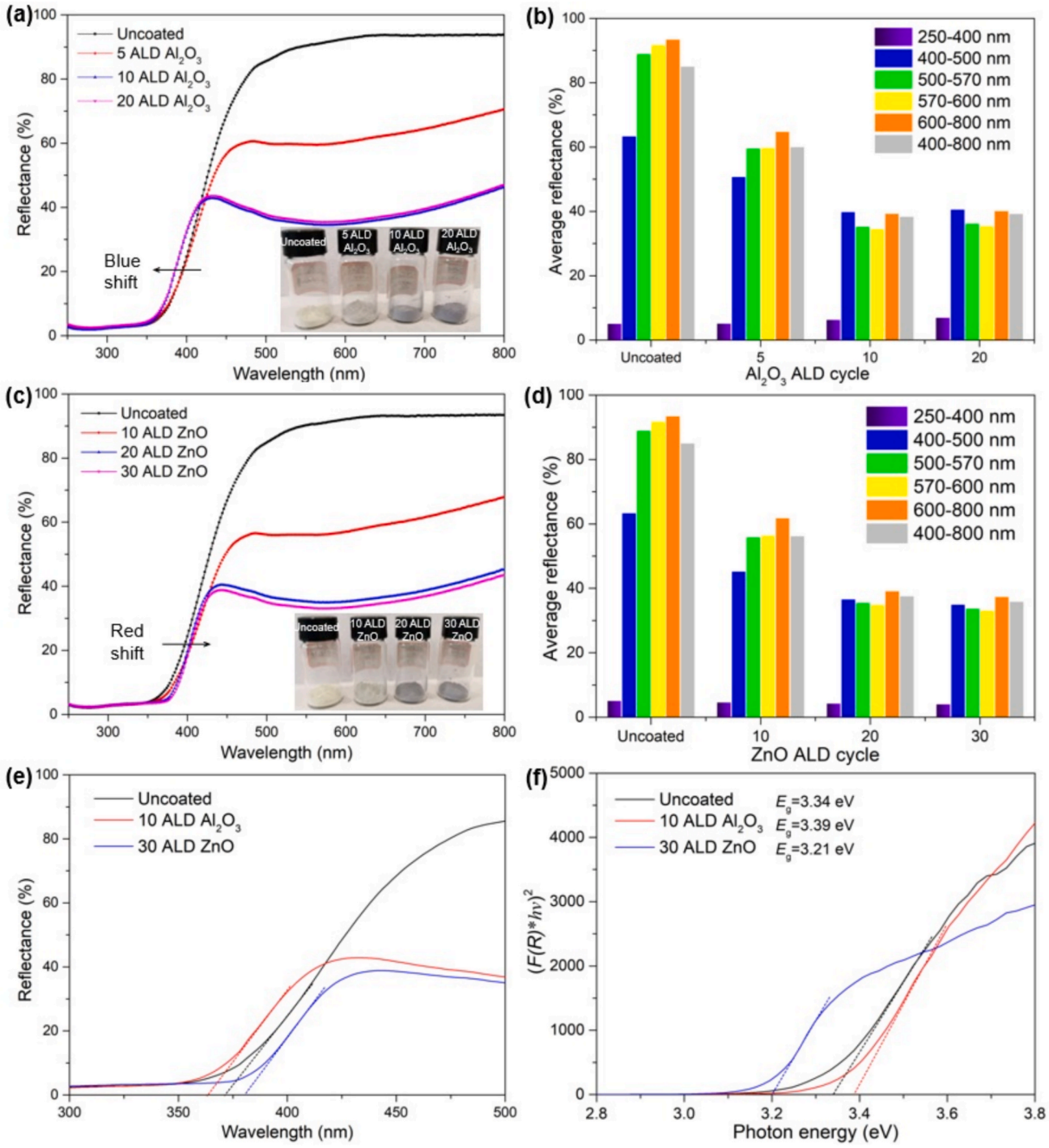

Fig. 11. Optical absorption property of ALD-coated CeO_2 nanoparticles. (a) DRS spectra in the range of 250–800 nm for the Al_2O_3-coated nanoparticles with different ALD cycles, with the inset showing the photograph of the coated nanoparticles. (b) Average reflectance calculated from (a). (c) DRS spectra in the range of 250–800 nm for the ZnO-coated nanoparticles with different ALD cycles, with the inset showing the photograph of the coated nanoparticles. (d) Average reflectance calculated from (c). (e) DRS spectra of CeO_2 nanoparticles, Al_2O_3-coated, and ZnO-coated CeO_2 nanoparticles in the wavelength of 300–500 nm. (f) Tauc plot analysis for band-gap calculation.

an increase of that value.

3.4. Mechanism analysis

The shifts in the UV-absorption band edges of the uncoated, 10 ALD Al_2O_3-coated, and 30 ALD ZnO-coated CeO_2 samples are carefully observed using valence band XPS (VB-XPS), as the results shown in Fig. 12. For a better observation, the zoomed areas of each sample as depicted in Fig. 12a are separately shown in Fig. 12b–d. According to the figures, the VB maximum (VBM) of uncoated CeO_2 nanoparticles was at 2.17 eV. On the other hand, CeO_2@10 ALD Al_2O_3 sample shows a lowering of VBM to 2.23 eV. The CeO_2@30 ALD ZnO sample exhibits VBM at 2.33 eV, showing a further dropping compared to the uncoated sample. The optical band-gap energies of the uncoated CeO_2, CeO_2@10 ALD Al_2O_3, and CeO_2@30 ALD ZnO sample are 3.34, 3.39, and 3.21 eV, respectively, which are obtained from Tauc plot analysis based on

Table 6
Band-gap energies of uncoated, 10 ALD Al_2O_3-coated, and 30 ALD ZnO-coated CeO_2 nanoparticles from Tauc plot analysis (Fig. 11f) and extrapolation from the reflectance onset wavelength (Fig. 11e).

Sample	Band-gap energy obtained from Tauc plot analysis (eV)	Band-gap energy from DRS data extrapolation (eV)
Uncoated CeO_2	3.34	3.33
CeO_2@10 ALD Al_2O_3	3.39	3.41
CeO_2@30 ALD ZnO	3.21	3.24

UV–vis DRS of the samples. Therefore, the proposed band structures of the ALD-coated CeO_2 nanoparticles are shown in Fig. 12e, which are based on the combination of VB-XPS and UV–vis DRS results. From the optical band-gap energies and VBM, the conduction band minima (CBM) of the uncoated CeO_2, CeO_2@10 ALD Al_2O_3, and CeO_2@30 ALD ZnO samples would occur at −1.17, −1.16, and −0.88 eV, respectively. For the Al_2O_3-coated sample, the dropping of VBM is ca. 0.06 eV while the CBM shows almost the same. Regarding the ZnO-coated sample, the dropping of CBM is 0.29 eV while that of VBM is 0.16 eV. Therefore, the blue shift of the UV-absorption band edge for the Al_2O_3-coated sample could be attributed to the dropping of VBM, while the red shift for the ZnO-coated sample is mainly due to the dropping of CBM.

Additionally, as the HRTEM analysis shown, the amorphous alumina nanofilm is deposited on CeO_2 cores, serving as an insulation layer. It has been reported that the ALD amorphous alumina layer shows a wild band gap of ca. 7.0 eV [60,61]. The insulated layer could hinder the excitation of electrons from the valence band, resulting an enlarged band-gap energy of CeO_2@Al_2O_3 nanoparticles. Regarding CeO_2@ZnO nanoparticles, the crystalline ZnO shell is coated on CeO_2 cores, and heterostructures are formed at the interface between CeO_2 core and ZnO

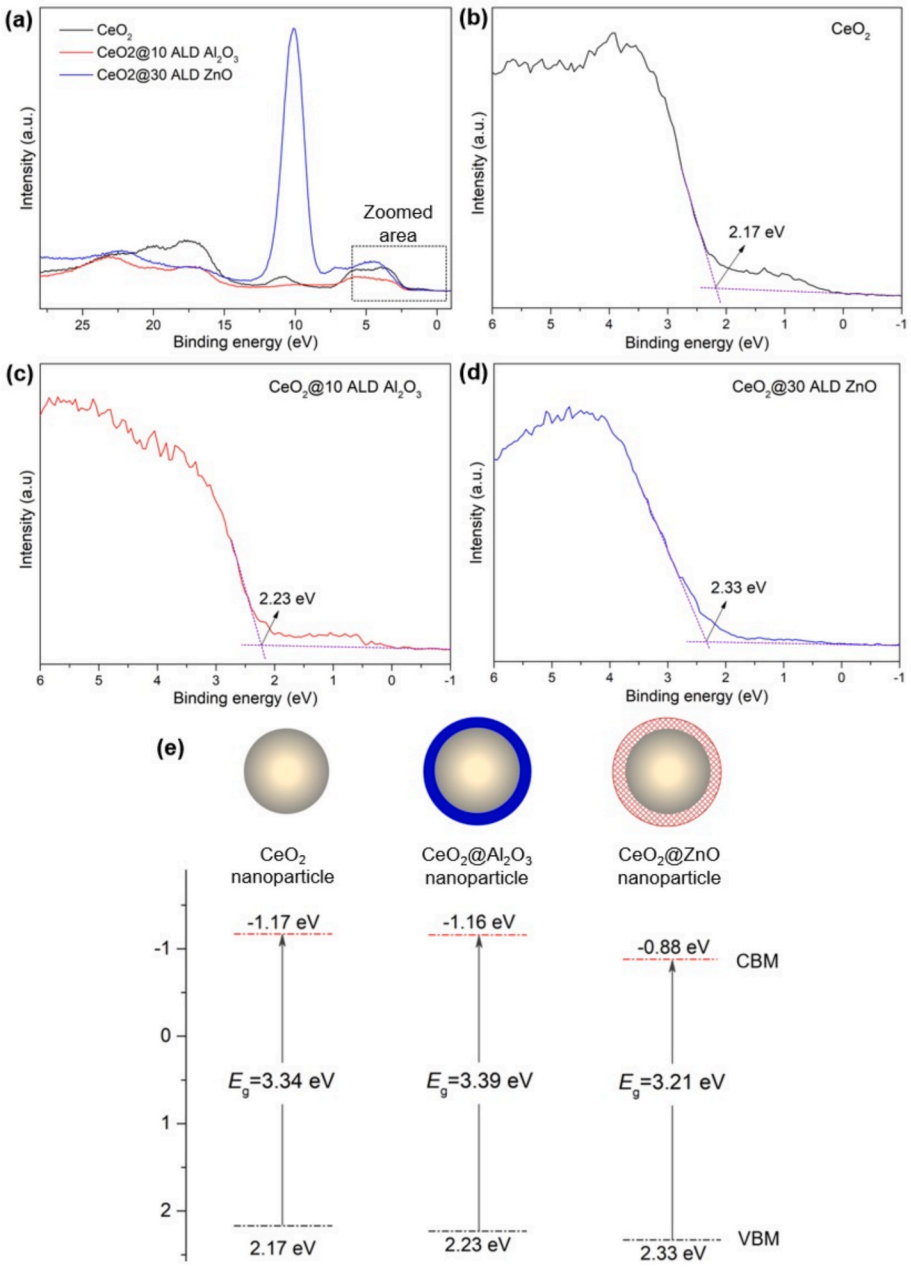

Fig. 12. (a) Valance band-XPS for uncoated and ALD-coated CeO_2 nanoparticles. (b) Valance band spectra for uncoated CeO_2 nanoparticles. (c) Valance band spectrum for CeO_2@Al_2O_3 nanoparticles. (d) Valance band spectrum for CeO_2@ZnO nanoparticles. (e) Schematic diagrams of the proposed band structures.

shell. It has been reported that the band gap of ZnO film is 3.3–3.5 eV, and the heterostructures of CeO_2/ZnO interface can be deemed as type II [62–64]. The blending of band structures could occur, which may result in valence band and conduction band getting closer to each other, thereby leading to a shrinkage of the effective band gap in the CeO_2@ZnO core@shell structure.

4. Conclusions

In summary, nanoscale Al_2O_3 and ZnO films are deposited on CeO_2 nanoparticles using atomic layer deposition with a custom fluidized bed reactor. As the number of ALD cycles increases, the colors of ALD-coated CeO_2 nanoparticles change from light yellow to light gray. The ALD-coated Al_2O_3 nanofilms that form CeO_2@Al_2O_3 core@shell structure are verified to be amorphous and rich in oxygen vacancies, while ZnO nanofilms are crystalline and form heterostructures at the interfaces between CeO_2 and ZnO. Both the Al_2O_3-coated and ZnO-coated CeO_2 nanoparticles show intense UV absorption. Compared to pristine CeO_2 nanoparticles, the absorption band edge of Al_2O_3-deposited nanoparticles after 10 ALD cycles shows a blue shift from 3.34 eV (pristine) to 3.39 eV, whereas that of ZnO-deposited nanoparticles after 30 ALD cycles exhibits a red shift to 3.21 eV. The blue shift of absorption band for Al_2O_3-modified nanoparticles can be ascribed to the existence of the insulation layer of amorphous alumina and the dropping of the valence band, which induces an enlarged band gap in CeO_2@Al_2O_3 core@shell structure. The red shift for ZnO-modified nanoparticles may result from the formation of heterostructures at the CeO_2/ZnO interfaces and the dropping of valence band, which leads to a shrinkage of the effective band gap. This work suggests that the color change of ceria nanoparticles can serve as a rapid indicator for preliminary assessment of the ALD process. Furthermore, it shows that the UV-absorption property of CeO_2 nanoparticles can be modulated by depositing nanofilms via particle ALD technique, enabling a feasible approach to utilize high-abundance rare earth elements in value-added applications.

CRediT authorship contribution statement

Guanghui Yan: Writing – original draft, Visualization, Validation, Methodology, Investigation, Formal analysis, Data curation, Conceptualization. **Heng Yu:** Writing – review & editing, Visualization, Investigation, Formal analysis, Data curation. **Lu Jin:** Writing – review & editing, Visualization, Investigation, Formal analysis. **Yi Ouyang:** Writing – review & editing, Methodology, Investigation, Formal analysis. **Guoxiang Chen:** Writing – review & editing, Investigation, Data curation. **Gaoshan Huang:** Writing – review & editing, Investigation, Funding acquisition, Formal analysis. **Xiangzhong Chen:** Writing – review & editing, Investigation, Formal analysis. **Jizhai Cui:** Writing – review & editing, Investigation, Formal analysis. **Xueqin Zuo:** Writing – review & editing, Methodology, Investigation, Formal analysis. **Zhihao Bao:** Writing – review & editing, Investigation, Formal analysis. **Yongfeng Mei:** Writing – review & editing, Methodology, Investigation, Funding acquisition, Formal analysis. **Jianjun Shi:** Writing – review & editing, Resources, Project administration, Methodology, Investigation, Funding acquisition, Formal analysis.

Declaration of competing interest

The authors declare that they have no known competing financial interests or personal relationships that could have appeared to influence the work reported in this paper.

Acknowledgments

The project is partially supported by the National Key Technologies R&D Program of China (No. 2021YFA0715302) and the National Natural Science Foundation of China (Nos. 12475259 and 62375054), and the Science and Technology Commission of Shanghai Municipality (No. 24520750200).

Appendix A. Supplementary material

Supplementary data to this article can be found online at https://doi.org/10.1016/j.apsusc.2025.164667.

Data availability

Data will be made available on request.

References

[1] J. Huang, H. Chen, B. Hao, W. Dai, S. Chen, Copolymerization strategy to prepare polymethyl methacrylate-based copolymer with broad-band ultraviolet shielding and luminescent down-shifting properties, J. Mater. Sci. 54 (2019) 14624–14633, https://doi.org/10.1007/s10853-019-03961-3.
[2] S. Das, P. Purkayastha, Gold nanocluster protection of protein from UVC radiation: a model study on bovine serum albumin, ACS Omega 2 (2017) 2451–2458, https://doi.org/10.1021/acsomega.7b00302.
[3] M.S. Paulo, B. Adam, C. Akagwu, I. Akparibo, R.H. Al-Rifai, S. Bazrafshan, F. Gobba, A.C. Green, I. Ivanov, S. Kezic, N. Leppink, T. Loney, A. Modenese, F. Pega, C.E. Peters, A.M. Prüss-Üstün, T. Tenkate, Y. Ujita, M. Wittlich, S.M. John, WHO/ILO work-related burden of disease and injury: protocol for systematic reviews of occupational exposure to solar ultraviolet radiation and of the effect of occupational exposure to solar ultraviolet radiation on melanoma and non-melanoma skin cancer, Environ. Int. 126 (2019) 804–815, https://doi.org/10.1016/j.envint.2018.09.039.
[4] M. Watson, D.M. Holman, M. Maguire-Eisen, Ultraviolet radiation exposure and its impact on skin cancer risk, Semin. Oncol. Nurs. 32 (2016) 241–254, https://doi.org/10.1016/j.soncn.2016.05.005.
[5] T. Masui, M. Yamamoto, T. Sakata, H. Mori, G. Adachi, Synthesis of BN-coated CeO_2 fine powder as a new UV blocking material, J. Mater. Chem. 10 (2000) 353–357, https://doi.org/10.1039/a906583k.
[6] P. Gago-Ferrero, M.S. Díaz-Cruz, D. Barceló, An overview of UV-absorbing compounds (organic UV filters) in aquatic biota, Anal. Bioanal. Chem. 404 (2012) 2597–2610, https://doi.org/10.1007/s00216-012-6067-7.
[7] C.S. Cockell, J. Knowland, Ultraviolet radiation screening compounds, Biol. Rev. 74 (1999) 311–345, https://doi.org/10.1017/s0006323199005356.
[8] I. Fajzulin, X. Zhu, M. Möller, Nanoparticulate inorganic UV absorbers: a review, J. Coat. Technol. Res. 12 (2015) 617–632, https://doi.org/10.1007/s11998-015-9683-2.
[9] Y. Kameda, K. Kimura, M. Miyazaki, Occurrence and profiles of organic sun-blocking agents in surface waters and sediments in Japanese rivers and lakes, Environ. Pollut. 159 (2011) 1570–1576, https://doi.org/10.1016/j.envpol.2011.02.055.
[10] Y. Li, W. Zhang, J. Niu, Y. Chen, Mechanism of photogenerated reactive oxygen species and correlation with the antibacterial properties of engineered metal-oxide nanoparticles, ACS Nano 6 (2012) 5164–5173, https://doi.org/10.1021/nn300934k.
[11] K.R. Singh, V. Nayak, T. Sarkar, R.P. Singh, Cerium oxide nanoparticles: properties, biosynthesis and biomedical application, RSC Adv. 10 (2020) 27194–27214, https://doi.org/10.1039/D0RA04736H.
[12] C. Xu, X. Qu, Cerium oxide nanoparticle: a remarkably versatile rare earth nanomaterial for biological applications, NPG Asia Mater. 6 (2014) e90, https://doi.org/10.1038/am.2013.88.
[13] W. Zhang, P. Zhang, Y. Wu, X. Li, X. Wang, M. Wang, S. Jin, W. Bi, Y. Zhao, W. Zhou, D. Zhang, Preparation of CeO_2 polishing powder and its performance and mechanism for chemical mechanical polishing of optical glass, ACS Appl. Mater. Interfaces 17 (2025) 20394–20410, https://doi.org/10.1021/acsami.4c21540.
[14] J. Cheng, S. Huang, Y. Li, T. Wang, L. Xie, X. Lu, RE (La, Nd and Yb) doped CeO_2 abrasive particles for chemical mechanical polishing of dielectric materials: experimental and computational analysis, Appl. Surf. Sci. 506 (2020) 144668, https://doi.org/10.1016/j.apsusc.2019.144668.
[15] Q. Li, L. Song, Z. Liang, M. Sun, T. Wu, B. Huang, F. Luo, Y. Du, C.-H. Yan, A review on CeO_2 -based electrocatalyst and photocatalyst in energy conversion, Adv. Energy Sustain. Res. 2 (2021) 2000063, https://doi.org/10.1002/aesr.202000063.
[16] T. Montini, M. Melchionna, M. Monai, P. Fornasiero, Fundamentals and catalytic applications of CeO_2 -based materials, Chem. Rev. 116 (2016) 5987–6041, https://doi.org/10.1021/acs.chemrev.5b00603.
[17] S. Parwaiz, M.M. Khan, D. Pradhan, CeO_2 -based nanocomposites: an advanced alternative to TiO_2 and ZnO in sunscreens, Mater. Express 9 (2019) 185–202, https://doi.org/10.1166/mex.2019.1495.
[18] Z.C. Orel, B. Orel, Optical properties of pure CeO_2 and mixed CeO_2/SnO_2 thin film coatings, Phys. Status Solidi B 186 (1994) K33–K36, https://doi.org/10.1002/pssb.2221860135.
[19] S.-Y. Zheng, A.M. Andersson-Fäldt, B. Stjerna, C.G. Granqvist, Optical properties of sputter-deposited cerium oxyfluoride thin films, Appl. Opt. 32 (1993) 6303, https://doi.org/10.1364/AO.32.006303.
[20] S. Yabe, T. Sato, Cerium oxide for sunscreen cosmetics, J. Solid State Chem. 171 (2003) 7–11, https://doi.org/10.1016/S0022-4596(02)00139-1.

[21] Y. Qi, J. Ye, S. Zhang, Q. Tian, N. Xu, P. Tian, G. Ning, Controllable synthesis of transition metal ion-doped CeO_2 micro/nanostructures for improving photocatalytic performance, J. Alloys Compd. 782 (2019) 780–788, https://doi.org/10.1016/j.jallcom.2018.12.111.

[22] B. Bao, Y. Sun, X. Li, L. Li, Y. Yu, Tuning the UV absorbing ability of CeO_2 nanoparticles with F− doping, FlatChem 39 (2023) 100494, https://doi.org/10.1016/j.flatc.2023.100494.

[23] Y. Li, X. Bian, W. Wu, H. Dong, Synthesis, characterization, and double shielding performance for ultraviolet and short-wave blue light of ceria-based materials, Ceram. Int. 50 (2024) 48592–48599, https://doi.org/10.1016/j.ceramint.2024.09.208.

[24] Y.-C. Huang, S.-H. Wu, C.-H. Hsiao, A.-T. Lee, M.H. Huang, Mild synthesis of size-tunable CeO_2 octahedra for band gap variation, Chem. Mater. 32 (2020) 2631–2638, https://doi.org/10.1021/acs.chemmater.0c00318.

[25] S.M. George, Atomic layer deposition: an overview, Chem. Rev. 110 (2010) 111–131, https://doi.org/10.1021/cr900056b.

[26] R.L. Puurunen, Surface chemistry of atomic layer deposition: a case study for the trimethylaluminum/water process, J. Appl. Phys. 97 (2005) 121301, https://doi.org/10.1063/1.1940727.

[27] Y. Hu, J. Lu, H. Feng, Surface modification and functionalization of powder materials by atomic layer deposition: a review, RSC Adv. 11 (2021) 11918–11942, https://doi.org/10.1039/D1RA00326G.

[28] Z. Li, J. Li, X. Liu, R. Chen, Progress in enhanced fluidization process for particle coating via atomic layer deposition, Chem. Eng. Process. - Process Intensif. 159 (2021) 108234, https://doi.org/10.1016/j.cep.2020.108234.

[29] J.R. Van Ommen, A. Goulas, Atomic layer deposition on particulate materials, Mater. Today Chem. 14 (2019) 100183, https://doi.org/10.1016/j.mtchem.2019.08.002.

[30] J.P.K. Seville, C.D. Willett, P.C. Knight, Interparticle forces in fluidisation: a review, Powder Technol. 113 (2000) 261–268, https://doi.org/10.1016/S0032-5910(00)00309-0.

[31] D. Longrie, D. Deduytsche, C. Detavernier, Reactor concepts for atomic layer deposition on agitated particles a review, J. Vac. Sci. Technol. A 32 (2014) 010802, https://doi.org/10.1116/1.4851676.

[32] S.W. Park, J. Woo Kim, H. Jong Choi, J. Hyung Shim, Vibration atomic layer deposition for conformal nanoparticle coating, J. Vac. Sci. Technol. A 32 (2014) 01A115, https://doi.org/10.1116/1.4845735.

[33] J.A. McComick, B.L. Cloutier, A.W. Weimer, S.M. George, Rotary reactor for atomic layer deposition on large quantities of nanoparticles, J. Vac. Sci. Technol. A 25 (2007) 67, https://doi.org/10.1116/1.2393299.

[34] D.M. King, J.A. Spencer, X. Liang, L.F. Hakim, A.W. Weimer, Atomic layer deposition on particles using a fluidized bed reactor with in situ mass spectrometry, Surf. Coat. Technol. 201 (2007) 9163–9171, https://doi.org/10.1016/j.surfcoat.2007.05.002.

[35] G. Yan, G. Huang, J. Shi, Y. Ouyang, X. Zuo, Z. Bao, Y. Mei, A Review on reactor design and surface modification of atomic layer deposition for functional nanoparticles, Adv. Mater. Interfaces 12 (2025) e00140, https://doi.org/10.1002/admi.202500140.

[36] K. Punia, G. Lal, S. Dalela, S.N. Dolia, P.A. Alvi, S.K. Barbar, K.B. Modi, S. Kumar, A comprehensive study on the impact of Gd substitution on structural, optical and magnetic properties of ZnO nanocrystals, J. Alloys Compd. 868 (2021) 159142, https://doi.org/10.1016/j.jallcom.2021.159142.

[37] J. Sahu, S. Kumar, F. Ahmed, P.A. Alvi, B. Dalela, D.M. Phase, M. Gupta, S. Dalela, Electrochemical and electronic structure properties of high-performance supercapacitor based on Nd-doped ZnO nanoparticles, J. Energy Storage 59 (2023) 106499, https://doi.org/10.1016/j.est.2022.106499.

[38] G. Ravina, S. Srivastava, N.K. Kumar, S. Gautam, M.A. Dalela, A.M. Ahmad, P.A Alvi Quraishi, Exploration of optical, structural, and electrochemical properties of ZnO/MWCNTs nanocomposites for usage in supercapacitor, J. Energy Storage 125 (2025) 116844, https://doi.org/10.1016/j.est.2025.116844.

[39] K. Punia, G. Lal, S.K. Barbar, S.N. Dolia, P.A. Alvi, S. Dalela, S. Kumar, Oxygen vacancies mediated cooperative magnetism in ZnO nanocrystals: a d0 ferromagnetic case study, Vacuum 184 (2021) 109921, https://doi.org/10.1016/j.vacuum.2020.109921.

[40] S. Saini, V. Dhayal, N.S. Leel, A.M. Ravina, S.Z. Quraishi, S. Hashmi, B.L. Dalela, P. A.A. Choudhary, Reinforcing the characteristics of recyclable PVA/PVDF polymer blends via ZnO nanofiller, Opt. Quantum Electron. 56 (2024) 1943, https://doi.org/10.1007/s11082-024-07816-3.

[41] S. Saini, S.Z. Hashmi, A.M. Quraishi, S. Dalela, B.L. Choudhary, S. Kumar, M. A. Ahmad, V. Khanna, P.A. Alvi, Tunability of characteristics of novel PMMA/ZnO/SnO_2 (PZS) polymer nanocomposites, Mater. Res. Innov. (2025) 1–16, https://doi.org/10.1080/14328917.2025.2501116.

[42] G.K. Williamson, W.H. Hall, X-ray line broadening from filed aluminium and wolfram, Acta Metall. 1 (1953) 22–31, https://doi.org/10.1016/0001-6160(53)90006-6.

[43] S.B. Dangi, S.Z. Hashmi, U. Kumar, B.L. Choudhary, A.E. Kuznetsov, S. Dalela, S. Kumar, S.N. Dolia, S. Kumar, B.F.I. Sofi, R. Darwesh, P.M.Z. Hasan, P.A. Alvi, Exploration of spectroscopic, surface morphological, structural, electrical, optical and mechanical properties of biocompatible PVA-GO PNCs, Diam. Relat. Mater. 127 (2022) 109158, https://doi.org/10.1016/j.diamond.2022.109158.

[44] K.K. Khichar, S.B. Dangi, V. Dhayal, U. Kumar, S.Z. Hashmi, V. Sadhu, B. L. Choudhary, S. Kumar, S. Kaya, A.E. Kuznetsov, S. Dalela, S.K. Gupta, P.A. Alvi, Structural, optical, and surface morphological studies of ethyl cellulose/graphene oxide nanocomposites, Polym. Compos. 41 (2020) 2792–2802, https://doi.org/10.1002/pc.25576.

[45] P.M.Z. Hasan, S. Saini, A.A. Melaibari, N.S. Leel, R. Aakansha, A.M. Darwesh, J. Quraishi, A.E. Singh, S.Z. Kuznetsov, S. Hashmi, P.A.A. Dalela, Tunable optical and structural characteristics with improved electrical properties of (PVA-GO-CuO) eco-friendly-polymer nanocomposites and their DFT study, Diam. Relat. Mater. 140 (2023) 110425, https://doi.org/10.1016/j.diamond.2023.110425.

[46] K.K. Khichar, S.B. Ravina, S.Z. Dangi, B.L. Hashmi, N.S. Choudhary, S. Leel, A. M. Dalela, S. Quraishi, B.F.I.S. Kumar, P.A.A. Aakansha, Tuning the properties of novel and biodegradable ethyl-cellulose (EC)/rGO nanocomposite, Int. J. Polym. Anal. Charact. 30 (2025) 711–727, https://doi.org/10.1080/1023666X.2025.2502811.

[47] E. Bêche, P. Charvin, D. Perarnau, S. Abanades, G. Flamant, Ce 3d XPS investigation of cerium oxides and mixed cerium oxide ($Ce_xTi_yO_z$), Surf. Interface Anal. 40 (2008) 264–267, https://doi.org/10.1002/sia.2686.

[48] S. Soni, S. Kumar, V.S. Vats, H.R. Khakhal, B. Dalela, S.N. Dolia, S. Kumar, P. A. Alvi, S. Dalela, Oxygen vacancies and defects induced room temperature ferromagnetic properties of pure and Fe-doped CeO_2 nanomaterials investigated using X-ray photoelectron spectroscopy, J. Electron Spectrosc. Relat. Phenom. 254 (2022) 147140, https://doi.org/10.1016/j.elspec.2021.147140.

[49] L. Truffault, M.-T. Ta, T. Devers, K. Konstantinov, V. Harel, C. Simmonard, C. Andreazza, I.P. Nevirkovets, A. Pineau, O. Veron, J.-P. Blondeau, Application of nanostructured Ca doped CeO_2 for ultraviolet filtration, Mater. Res. Bull. 45 (2010) 527–535, https://doi.org/10.1016/j.materresbull.2010.02.008.

[50] E. Paparazzo, On the curve-fitting of XPS Ce(3d) spectra of cerium oxides, Mater. Res. Bull. 46 (2011) 323–326, https://doi.org/10.1016/j.materresbull.2010.11.009.

[51] M.V. Ganduglia-Pirovano, A. Hofmann, J. Sauer, Oxygen vacancies in transition metal and rare earth oxides: current state of understanding and remaining challenges, Surf. Sci. Rep. 62 (2007) 219–270, https://doi.org/10.1016/j.surfrep.2007.03.002.

[52] D.M. King, X.H. Liang, C.S. Carney, L.F. Hakim, P. Li, A.W. Weimer, Atomic layer deposition of UV-absorbing ZnO films on SiO_2 and TiO_2 nanoparticles using a fluidized bed reactor, Adv. Funct. Mater. 18 (2008) 607–615, https://doi.org/10.1002/adfm.200700705.

[53] X.L. Li, C. Li, Y. Zhang, D.P. Chu, W.I. Milne, H.J. Fan, Atomic layer deposition of ZnO on multi-walled carbon nanotubes and its use for synthesis of CNT–ZnO heterostructures, Nanoscale Res. Lett. 5 (2010) 1836–1840, https://doi.org/10.1007/s11671-010-9721-z.

[54] J. Tauc, Optical properties and electronic structure of amorphous Ge and Si, Mater. Res. Bull. 3 (1968) 37–46, https://doi.org/10.1016/0025-5408(68)90023-8.

[55] J. Tauc, R. Grigorovici, A. Vancu, Optical properties and electronic structure of amorphous germanium, Phys. Status Solidi B 15 (1966) 627–637, https://doi.org/10.1002/pssb.19660150224.

[56] J.B. Coulter, D.P. Birnie, Assessing tauc plot slope quantification: ZnO thin films as a model system, Phys. Status Solidi B 255 (2018) 1700393, https://doi.org/10.1002/pssb.201700393.

[57] P.S. Kubelka, F. Munk, Ein Beitrag Zur Optik Der Farbanstriche, Z. Für Tech. Phys. 12 (n.d.) 593–601.

[58] R. López, R. Gómez, Band-gap energy estimation from diffuse reflectance measurements on sol–gel and commercial TiO_2: a comparative study, J. Sol-Gel Sci. Technol. 61 (2012) 1–7, https://doi.org/10.1007/s10971-011-2582-9.

[59] P. Makuła, M. Pacia, W. Macyk, How to correctly determine the band gap energy of modified semiconductor photocatalysts based on UV–Vis spectra, J. Phys. Chem. Lett. 9 (2018) 6814–6817, https://doi.org/10.1021/acs.jpclett.8b02892.

[60] C. Fares, F. Ren, M.J. Tadjer, J. Woodward, M.l.A. Mastro, B.N. Feigelson, C. R. Eddy, S.J. Pearton, Band offset determination for amorphous Al_2O_3 deposited on bulk AlN and atomic-layer epitaxial AlN on sapphire, Appl. Phys. Lett. 117 (2020) 182103.

[61] J.W. Liu, M.Y. Liao, M. Imura, Y. Koide, Band offsets of Al_2O_3 and HfO_2 oxides deposited by atomic layer deposition technique on hydrogenated diamond, Appl. Phys. Lett. 101 (2012) 252108, https://doi.org/10.1063/1.4772985.

[62] S. Boonphan, S. Prachakiew, A. Prasatkhetragarn, A. Klinbumrung, Investigation of crystallography and charge transfer dynamics of CeO_2–ZnO nanocomposites prepared via facial thermal decomposition, Electron. Mater. Lett. 21 (2025) 162–176, https://doi.org/10.1007/s13391-024-00539-3.

[63] X. Ai, S. Yan, C. Lin, K. Lu, Y. Chen, L. Ma, Facile fabrication of highly active CeO_2@ZnO nanoheterojunction photocatalysts, Nanomaterials 13 (2023) 1371, https://doi.org/10.3390/nano13081371.

[64] C.-H. Zhai, R.-J. Zhang, X. Chen, Y.-X. Zheng, S.-Y. Wang, J. Liu, N. Dai, L.-Y. Chen, Effects of Al doping on the properties of ZnO thin films deposited by atomic layer deposition, Nanoscale Res. Lett. 11 (2016) 407, https://doi.org/10.1186/s11671-016-1625-0.